



Phase Relationship in the Zr-Mo-Fe(O) System (Zr > 30 at.%) at 1000 °C

Yule Ren¹ · Jinming Zhu¹ · Jianlie Liang^{1,2} · Jinfeng Ling¹ · Guangfeng Li¹ · Wen Qin³ · Liyang Fang⁴ · Xuehong Cui¹ · Yuechun Fu² · Yiyuan Tang⁵

Submitted: 23 June 2022 / in revised form: 28 May 2023 / Accepted: 5 June 2023 / Published online: 8 August 2023
© ASM International 2023

Abstract The impact of oxygen impurity on phase relationships in the Zr-Mo-Fe system (Zr > 30 at.%) at 1000 °C was investigated by means of x-ray diffraction, scanning electron microscopy, and energy-dispersive spectroscopy analysis. An oxygen-stabilized ternary compound γ -Zr₂(Mo,Fe), derived from Ti₂Ni type Zr₄Fe₂O, with cell parameter of $a = 1.2213$ nm was observed to be present in the investigated Zr-Mo-Fe alloys. The phase relationships of the Zr-Mo-Fe (O) system at 1000 °C in the Zr-rich corner consist of 3 four-phase regions, i.e., [β Zr + λ -Zr(Mo,Fe)₂ + γ -Zr₂(Mo,Fe) + ZrMo₂], [β Zr + λ -Zr(Mo,Fe)₂ + γ -Zr₂(Mo,Fe) + Liquid], and [λ -Zr(Mo,Fe)₂ + γ -Zr₂(Mo,Fe) + Liquid + ZrFe₂]. The previously detected Zr₉Mo₄Fe compound was not observed in this work.

Keywords intermetallics · phase equilibria · Zr-Mo-Fe alloys

1 Introduction

Zirconium alloys are widely used as cladding and structural materials in nuclear reactors due to their low neutron absorption cross section, excellent corrosion and creep resistance in the harsh reactor environment.^[1] In a loss-of-coolant accident (LOCA) scenario, the temperature of the reactor core rapidly increases, leading to the evaporation of coolant. During a LOCA transient, zirconium cladding tubes undergo a violent reaction with steam, resulting in the formation of a surface oxide layer of ZrO₂, an oxygen-stabilized layer of α -Zr solution, and diffusion of oxygen into the underlying β Zr substrate, if the core temperature is higher than that of the alpha-to-beta transformation.^[2, 3] At 1000 °C, the oxygen content in the β Zr can reach 0.7 wt.%.^[2] The oxidation process can degrade the ductility of the cladding tube and increase its risk of failure.^[4] In the development of a zirconium alloy, oxygen has always been used as a strengthening alloying element. The content of the diluted oxygen ranges from 0.06 to 0.16 wt.%, depending on the specific alloy series.^[5] For example, the oxygen content in Zircaloy-2 and Zircaloy-4 ranges from 0.09 to 0.16 wt.%, while M5TM (a trademark of Framatome) and ZirloTM (a trademark of Westinghouse) alloys have an oxygen content of 0.125 wt.%. E110 alloy has an oxygen content of 0.06 wt.%, and E635 alloy has an oxygen content of 0.08 wt.%, respectively.^[5] The addition of oxygen as an alloying element is believed to fully dissolve in the Zr matrix and form a Zr(O) solution in the commercial zirconium alloys. There has been little

✉ Jinming Zhu
jmzhu@alum.imr.ac.cn

✉ Jianlie Liang
Liangjianlie@gxmzu.edu.cn

¹ Guangxi Colleges and Universities Key Laboratory of Environmental-friendly Materials and New Technology for Carbon Neutralization, Guangxi Key Laboratory of Advanced Structural Materials and Carbon Neutralization, Guangxi Minzu University, Nanning 530105, Guangxi, P. R. China

² Guangxi Key Laboratory of Processing for Non-ferrous Metals and Featured Materials, Guangxi University, Nanning 530004, Guangxi, P. R. China

³ School of Science, Guangdong University of Petrochemical Technology, Maoming 525000, Guangdong, P. R. China

⁴ College of Physics Science and Technology, Guangxi University, Nanning 530004, Guangxi, P. R. China

⁵ School of Mathematics and Physics, Guangxi Minzu University, Nanning 530006, Guangxi, P. R. China

research focusing on the phase relationships of zirconium alloys with varying levels of oxygen. It is interesting to investigate whether the precipitates in the cladding tubes change when the oxygen content increases during a LOCA transient. The present work will provide a new perspective on this issue.

The Zr-Mo-Fe system is an important subsystem in zirconium alloys. Previous studies showed that the addition of Mo improves the creep resistance of these alloys.^[6–8] Zr-Excel alloys (Zr-3.5Sn-0.8Mo-0.8Nb-0.1Fe) have been found to exhibit excellent creep resistance.^[9] Lee et al. conducted a comparative study of ZirloTM alloys and Mo diluted ZirloTM alloys.^[10] Their findings showed that after recrystallization at 570, 600, and 650 °C for 8 h, the ZirloTM alloy with Mo addition exhibited a higher corrosion rate in 360 °C water containing 0.01 mol/L LiOH under saturated pressure conditions at 18.8 MPa.^[10] When the recrystallization time was extended to 32 h at 600 °C, the Mo-diluted ZirloTM alloys showed corrosion resistance equivalent to that of the ZirloTM alloys.^[10] Recently, Niculina et al. observed that the 0.1% Mo addition in the E635 alloys (Zr-1.2Sn-1.0Nb-0.35Fe) greatly reduced its hydrogenation and propensity for nodular corrosion. The researchers found that Mo prefers to dissolve in Laves phase Zr(Nb,Fe)₂ to form Zr(Nb,Fe,Mo)₂ rather than forming cubic ZrMo₂ compound.^[11] Our previous research has shown that precipitate in the Zr-Excel alloy was ZrMo₂.^[12]

The Zr-Mo binary system and the Fe-Mo binary system have been extensively studied. The latest accepted Zr-Fe binary system is that reported by Stein et al.^[13] The stable intermetallics in the Zr-Fe alloys include cubic ZrFe₂, hexagonal ZrFe₂, tetragonal Zr₂Fe, and orthorhombic Zr₃Fe. The previous known cubic Zr₆Fe₂₃ phase on the Fe-rich side has been shown to be stabilized by oxygen.^[13] In the Zr-Mo system, there is only one intermediate phase, which is ZrMo₂. This phase has C15 structure type and is formed by peritectic reaction: L + (Mo) → ZrMo₂ at 1921 °C.^[14] In the Fe-Mo system, there are four intermetallic phases, which are λ, R, μ, and σ.^[15] The λ phase is stable below 927 °C with the constant composition of 33.3 at.% Mo. The R phase is stable from 1200 to 1488 °C with the maximum composition range from 33.9 to 38.5 at.% Mo. The μ phase is stable below 1370 °C in composition range from 39.0 to 44.0 at.% Mo. The σ phase is stable from 1235 to 1611 °C with the maximum composition range from 33.9 to 38.5 at.% Mo.^[15]

Gruzdeva and Tregubov conducted a study on four partial isothermal sections in the Zr-rich corner of the Zr-Mo-Fe system at 1000, 900, 800, 700 °C, respectively.^[16] No ternary compound was reported in this early work.^[16] According to their results, bcc solid solution βZr is in equilibrium with ZrMo₂ and liquid at 1000 °C. At 900 °C, the liquid disappears, and bcc βZr is in equilibrium with

ZrMo₂ and ZrFe₂. At 800 °C, hcp αZr appears and equilibrates with βZr. βZr is still in equilibrium with ZrMo₂ and ZrFe₂ with its domain shrinking.^[16] In 1973, Rogl et al. reported a ternary compound Zr₉Mo₄Fe.^[17] This ternary compound has hexagonal Hf₉Mo₄B structure type with Hf and B positions occupied by Zr and Fe, respectively.^[17] Another ternary phase λ-Zr(Mo,Fe)₂ with C14 hexagonal structure and Zr content at 33 at.% and Mo varying from 6 to 53 at.% was found in this system.^[18] Zinkevich and Mattern conducted a thermodynamic assessment of this system based on limited experimental information.^[18] In the process of preparing this manuscript, we found that Du et al. had reported an isothermal section of the Zr-Mo-Fe ternary system at 1000 °C.^[19] They did not observe the ternary compound Zr₉Mo₄Fe, and did not report on the effect of impurity oxygen on the phase relationship in their work.^[19]

The initial purpose of this work was to investigate the phase equilibria in the Zr-Mo-Fe system. The uptake of oxygen during the melting process results in a change of the phase relationship from the ternary Zr-Mo-Fe system to the quaternary Zr-Mo-Fe-O system. In light of the oxygen alloying effect and the rapid oxidation of zirconium-based cladding tubes during a transient LOCA scenario, it is important to develop an understanding of the phase relationship in Zr-Mo-Fe(O) ternary alloys.

2 Experimental Details

Nuclear grade sponge Zr (Zr > 99.8 wt.%, with main impurities of Fe 700 ppm, and O 700 ppm), pure Mo (99.95 wt.%), and Fe (99.95 wt.%) were used as starting materials. Ingots (4 g) were arc melted in an environment of pure argon (99.99 %). The alloy buttons were melted five times to guarantee homogeneity. After melting, the average weight gain rate of the alloy ingots is less than 0.5 wt.%. As-prepared buttons were sealed in vacuum quartz tubes with an inner diameter Ø10 mm and length 80 mm. The buttons were directly annealed at 1000 °C for 20 days, followed by a water quench. The quartz tubes were evacuated by using an Oil Sealed Rotary Vane Pump. The vacuum after evacuation was about 10 Pa. The quartz tubes were sealed by using oxy-acetylene flame, and preserved unbroken during the heat treatment. Thus, the influence of the retained oxygen in the sealed quartz tube on the amount of oxygen in the quenched alloy is negligible. The oxygen content for the selected alloys was measured by using inert gas fusion-infrared absorption method. The results show that the oxygen contents of three selected alloys are, 1200 ppm, 3400 ppm, and 4800 ppm, respectively. For the reader's convenience, a representation of the alloy compositions fabricated in this work was

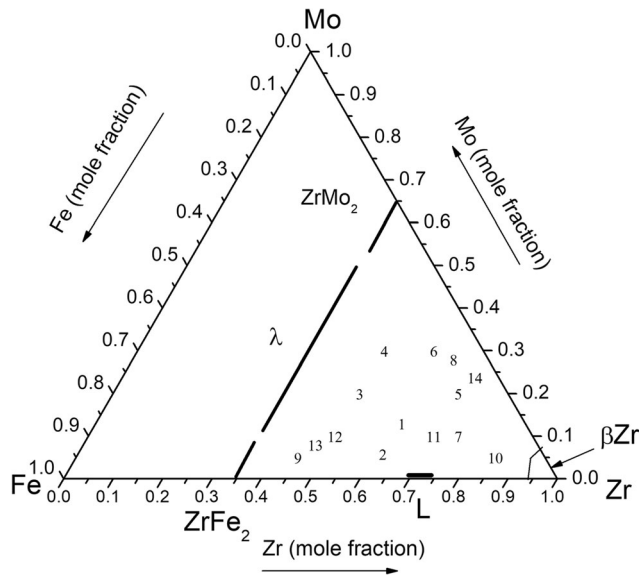


Fig. 1 Compositional map for the alloys fabricated in this work. Composition point of alloy 15 is not included in the map as it overlaps to that of alloy 1. Composition point of alloy 16 is not presented as it is too close to alloy 12

presented in Fig. 1. The designed alloy composition could be found in Table 1.

The annealed alloys were characterized by x-ray diffraction (XRD). The XRD was carried out on the XD–3 diffractometer or Bruker Advance-D8 with CuK α radiation and graphite monochromator. The indexing results were obtained by using Dicvol2006 software.^[20–22] The metallographic specimens were prepared by mechanical grinding and polishing, but without etching. Microstructural observation and compositional analysis were carried out on a Scanning Electron Microscopy (SEM, EVO 18) coupled with an energy dispersive X-ray spectrometer (EDX, Bruker 5010). The compositions of the bulk alloys and the identified phases were obtained by area scan mode and dot scan mode, respectively, with ZAF corrections. Microstructure analyses of alloys 15–16 were performed by using electron probe microanalyzer (EPMA, JEOL JXA-8230). The acceleration voltage was 20 kV. Standards were used for the concentration calculation of the Zr, Mo, and Fe elements. For the element mapping an area of 200 \times 200 μm was selected. The composition point was designed as 500 \times 500 by using one step per 0.4 μm . In

Table 1 The results of Zr-Mo-Fe alloys annealed at 1000 $^{\circ}\text{C}$ for 20 days analyzed by using XRD and SEM/EDS or EPMA

No.	Alloy compositions, at.%						Phase identified	Measured compositions, at.%		
	Nominal			Measured				Zr	Mo	Fe
	Zr	Mo	Fe	Zr	Mo	Fe				
1 ^a	62	13	25				γ -Zr ₂ (Mo,Fe)	57.5	16.7	25.8
							λ -Zr(Mo,Fe) ₂	36.1	37.4	26.5
							β Zr	90.4	4.7	4.9
							Zr ₂ Fe	72.7	0.8	26.5
1	62	13	25	63.3	15.0	24.7	γ -Zr ₂ (Mo,Fe)	63.3 (0.8)	9.7 (0.2)	27.0 (0.5)
							λ -Zr(Mo,Fe) ₂	37.8 (0.1)	28.6 (0.3)	33.6 (0.4)
							β Zr	89.5 (0.5)	6.7 (0.1)	3.8 (0.3)
2 ^{b,e}	63	6	33	63.1	5.6	31.3	γ -Zr ₂ (Mo,Fe)	66.5 (0.3)	4.5 (0.0)	29.0 (0.3)
							λ -Zr(Mo,Fe) ₂	36.5 (0.6)	10.8 (0.5)	52.7 (1.1)
3	50	20	30	52.3	18.0	29.7	λ -Zr(Mo,Fe) ₂	37.8 (1.2)	29.4 (0.4)	32.8 (1.6)
							γ -Zr ₂ (Mo,Fe)	63.0 (1.2)	9.7 (0.1)	27.3 (1.3)
							L	78.0	1.8	20.2
							β Zr ^c	92.1 (0.7)	4.0 (0.1)	3.9 (0.7)
							Zr ₂ Fe ^c	67.4	0.4	32.2
4	50	30	20	49.9	29.4	20.7	λ -Zr(Mo,Fe) ₂	38.0 (0.4)	39.0 (2.8)	23.0 (2.4)
							γ -Zr ₂ (Mo,Fe)	63.2 (0.8)	12.0 (0.0)	24.8 (0.9)
							β Zr	89.5 (0.2)	7.7 (0.0)	2.8 (0.2)
5 ^{e,f}	70	20	10	72.9	17.5	9.6	ZrMo ₂	37.6 (0.1)	49.5 (0.1)	13.0 (0.0)
							γ -Zr ₂ (Mo,Fe)	63.1 (0.2)	12.6 (0.1)	24.3 (0.4)
							β Zr	89.7 (0.6)	7.7 (0.2)	2.6 (2.6)
							Mo	n.d.		
6 ^c	60	30	10	59.3	29.4	11.3	ZrMo ₂	36.8 (0.1)	53.0 (2.3)	10.0 (2.6)
							γ -Zr ₂ (Mo,Fe)	63.6 (0.8)	14.6 (0.3)	21.8 (1.0)

Table 1 continued

No.	Alloy compositions, at.%						Phase identified	Measured compositions, at.%		
	Nominal			Measured				Zr	Mo	Fe
	Zr	Mo	Fe	Zr	Mo	Fe				
7	75	10	15	73.9	11.4	14.7	β Zr	90.9 (0.2)	7.3 (0.4)	1.8 (0.1)
							λ -Zr(Mo,Fe) ₂	38.9 (0.2)	35.0 (0.8)	26.1 (1.0)
							γ -Zr ₂ (Mo,Fe)	63.8 (0.3)	11.1 (0.4)	25.1 (0.2)
8	65	28	7	65.3	28.0	6.7	β Zr	90.1 (0.4)	7.0 (0.1)	2.9 (0.4)
							ZrMo ₂	37.0	52.9	10.1
							γ -Zr ₂ (Mo,Fe)	60.9	15.0	25.1
9 ^g	45	5	50	n.d.	n.d.	n.d.	β Zr	90.6	7.8	1.6
							λ -Zr(Mo,Fe) ₂	35.2	6.5	58.3
							γ -Zr ₂ (Mo,Fe)	65.7	3.3	31.0
10	85	5	10	83.8	5.1	11.1	ZrFe ₂	34.6	5.0	60.4
							γ -Zr ₂ (Mo,Fe)	66.3 (0.2)	6.3 (0.1)	27.4 (0.2)
							β Zr	91.6 (0.2)	4.8 (0.2)	3.6 (0.5)
11	70	10	20	72.0	8.7	19.3	λ -Zr(Mo,Fe) ₂	38.1 (0.2)	29.9 (0.3)	32.0 (0.7)
							γ -Zr ₂ (Mo,Fe)	64.0 (0.1)	9.8 (0.2)	26.2 (0.2)
							β Zr	90.5 (0.5)	6.4 (0.2)	3.1 (0.4)
12	50	10	40	50.6	9.6	39.8	λ -Zr(Mo,Fe) ₂	36.3 (0.4)	13.8 (0.4)	49.9 (0.3)
							γ -Zr ₂ (Mo,Fe)	65.4 (0.1)	5.9 (0.2)	28.7 (0.3)
							L (Zr ₃ Fe) ^d	74.6 (1.5)	1.7 (0.3)	23.7 (1.9)
13	47	8	45	47.0	8.2	44.8	λ -Zr(Mo,Fe) ₂	37.4 (0.7)	11.1 (0.1)	52.5 (0.6)
							γ -Zr ₂ (Mo,Fe)	63.8 (1.3)	4.8 (0.2)	29.4 (0.7)
							L		n.d.	
14	75	25	5	74.7	24.2	5.1	ZrMo ₂	36.1	52.8	11.1
							β Zr	90.5	7.1	2.5
							γ -Zr ₂ (Mo,Fe)	62.9	14.8	22.3
15 ^h	63	13	24	n.d.	n.d.	n.d.	λ -Zr(Mo,Fe) ₂	36.15	30.38	33.47
							γ -Zr ₂ (Mo,Fe)	61.26 (0.09)	10.16 (0.07)	28.58 (0.02)
							β Zr	88.25 (0.10)	7.34 (0.14)	4.41 (0.09)
16 ^h	55	12	43	n.d.	n.d.	n.d.	L		n.d.	
							Zr ₂ Fe ⁱ	69.3 (1.8)	0.9 (0.2)	29.8 (2.0)
							L	63.98	0.45	35.58
							λ -Zr(Mo,Fe) ₂	32.57	14.66	52.77
							γ -Zr ₂ (Mo,Fe)	61.77	6.34	31.88
							λ -Zr(Mo,Fe) ₂	36.36	37.09	26.54

^aAs-cast alloy^bAnnealed at 900 °C for 10 days^cLiquid was observed clearly in this alloy. β Zr and Zr₂Fe are the solidification products of liquid^dLiquid composition was measured by the point scan mode. This composition showed that liquid solidifies into Zr₃Fe after quenching^eOxygen content in alloys 2, 5, and 6 is 1200 ppm, 3400 ppm, 4800 ppm, respectively^hThis alloy was not in equilibrium. Un-melted Mo was observed by XRD but not in the analysis region of SEM^gAnother batch of alloy 9 annealed at 1000 °C for 5 days, well established grain boundaries indicated equilibrium reached. The compositions of the identified phases in the new alloy are nearly identical to those of alloy annealed at 1000 °C for 20 days^hAnnealed at 1000 °C for 7 days. Composition measured by EPMAⁱZr₂Fe is the solidification product of liquid

The digits in parenthesis are the standard deviation. For the compositions with only one measurement, no standard deviation was provided

the present work, element maps were presented along with the element intensity data-bar, which was generated by the system software based on the counts of characteristic x-ray lines. These values were used to specify the image color contour, which characterized the distribution of element concentration. For the metallographic quantitative analysis, software Fiji/Image J was utilized.^[23]

3 Results and Discussions

Table 1 presents the results of alloys investigated using XRD and SEM/EDS. The composition of alloys 15-16 was measured using EPMA. A new oxygen-stabilized ternary compound, denoted as γ -Zr₂(Mo,Fe), was observed in present work.

Large amount of phase γ -Zr₂(Mo,Fe) and minor fraction of λ -Zr(Mo,Fe)₂ were observed in alloy 2. This alloy was annealed at 900 °C for 10 days. This temperature was chosen to ensure the synthesis of solid γ -Zr₂(Mo,Fe) as liquid would appear at 1000 °C. Figure 2(a) is the back-scattered electron (BSE) image of the microstructure of this

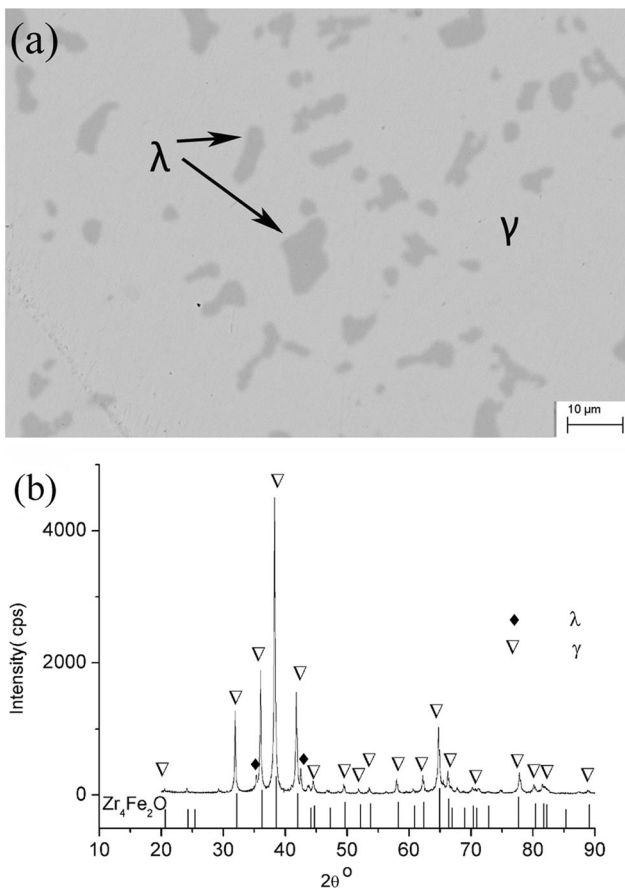


Fig. 2 Nearly single γ phase present in alloy 2 annealed at 900 °C for 10 days, (a) BSE image of microstructure, and (b) x-ray diffraction pattern

Table 2 The observed diffraction peaks and indexing results of new ternary compound γ -Zr₂(Mo,Fe)

H	K	L	2 θ -Obs.	d-Obs., nm	2 θ -Cal.	d-Cal., nm	Intensity
3	3	1	32.040	0.27912	32.031	0.27919	23.4
4	2	2	36.119	0.24848	36.113	0.24852	38.3
3	3	3	38.380	0.23435	38.379	0.23435	100
5	1	1			38.379	0.23435	
4	4	0	41.920	0.21534	41.923	0.21533	41.8
5	3	1	43.921	0.20598	43.935	0.20592	2.8
4	4	2	44.598	0.20301	44.589	0.20305	3.3
6	0	0			44.589	0.20305	
6	2	2	49.582	0.18371	49.58	0.18371	4.1
4	4	4	51.923	0.17596	51.938	0.17591	2.5
5	5	1	53.661	0.17067	53.658	0.17067	2.9
7	1	1			53.658	0.17067	
5	5	3	58.080	0.15869	58.071	0.15871	7.4
7	3	1			58.071	0.15871	
7	3	3	62.299	0.14892	62.28	0.14896	8.5
6	6	0	64.841	0.14368	64.829	0.14370	33.6
8	2	2			64.829	0.14370	
5	5	5	66.340	0.14079	66.332	0.14081	8.5
7	5	1			66.332	0.14081	
7	5	3	70.261	0.13386	70.261	0.13386	3.1
9	1	1			70.261	0.13386	
8	4	2	70.741	0.13307	70.745	0.13307	1.9
7	5	5	77.861	0.12259	77.856	0.12259	13.9
7	7	1			77.856	0.12259	
9	3	3			77.856	0.12259	
8	6	2	80.201	0.11959	80.179	0.11962	5
10	2	0			80.179	0.11962	
7	7	3	81.560	0.11794	81.565	0.11793	4.4
9	5	1			81.565	0.11793	
6	6	6	82.041	0.11737	82.025	0.11738	3.2
10	2	2			82.025	0.11738	
7	7	5	88.921	0.10998	88.89	0.11001	2
11	1	1			88.89	0.11001	

Cal. abbreviation of calculated, Obs. abbreviation of observed. M (14) = 30.3.

alloy, in which two phases are clearly identified. The white-gray phase with a composition of Zr_{66.5}Mo_{4.5}Fe_{29.0} represents ternary γ -Zr₂(Mo,Fe) compound, while the black-gray phase with a composition of Zr_{36.5}Mo_{10.8}Fe_{52.7} is identified as λ -Zr(Mo,Fe)₂ with C14-type hexagonal structure. Figure 2(b) is the x-ray diffraction pattern of this alloy. By subtracting the peaks of λ -Zr(Mo,Fe)₂ the remaining diffraction peaks were found to match well with those of the Ti₂Ni type compound Zr₄Fe₂O.^[24] Considering the oxygen contamination present in this work, which will

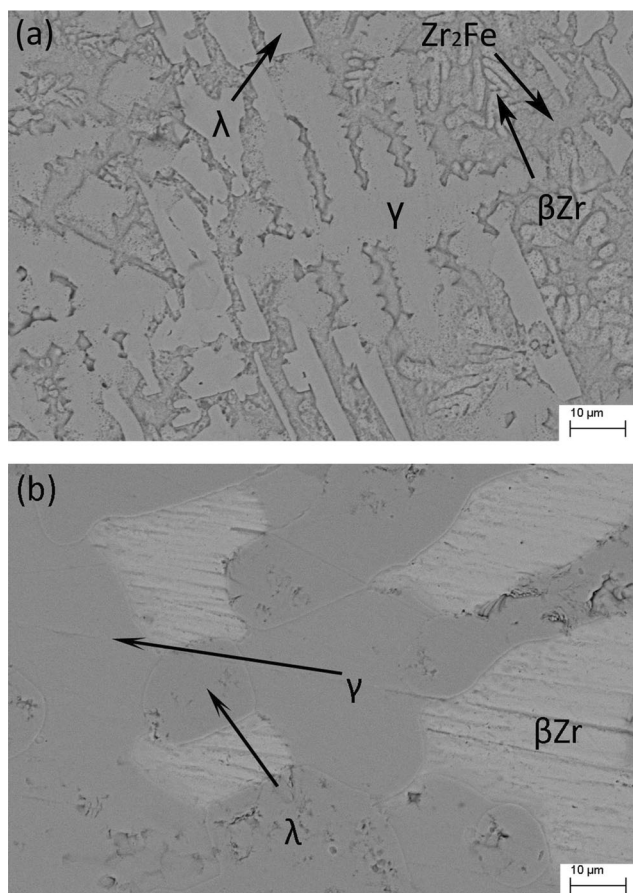


Fig. 3 The microstructure of alloy 1 ($Zr_{62}Mo_{13}Fe_{25}$), (a) as-cast, and (b) annealed at 1000 °C for 20 days

be discussed in detail later in the text, we suggest that the γ - $Zr_2(Mo,Fe)$ compound is derived from Zr_4Fe_2O with Fe partially replaced by Mo. DicoVol^[20–22] software was used to index the observed 14 peaks for this γ phase. The results showed that γ phase has a fcc structure with a cell parameter of $a = 1.2213$ nm, as shown in Table 2.

This Ti_2Ni type compound was first observed in the as-cast alloy 1 ($Zr_{62}Mo_{13}Fe_{25}$), as shown in Fig. 3(a). The composition of the dendrite γ phase in this alloy is $Zr_{57.5}Mo_{16.7}Fe_{25.8}$. No the ternary phase with such composition was reported in the Zr-Mo-Fe system. Thus, this phase was initially thought to be a new ternary compound. Apart from γ phase, λ - $Zr(Mo,Fe)_2$ with the composition of $Zr_{36.1}Mo_{37.4}Fe_{26.5}$, βZr with the composition of $Zr_{90.4}Mo_{4.7}Fe_{4.9}$, and Zr_2Fe with the composition of $Zr_{72.7}Mo_{0.8}Fe_{26.5}$ were observed in the as-cast alloy. After being subjected to heat treatment at 1000 °C for 20 days, a microstructure with coarse and well-rounded grains was obtained for alloy 1, as shown in Fig. 3(b). This microstructure indicates the thermodynamic equilibrium has been reached for this alloy, with λ - $Zr(Mo,Fe)_2$ and γ observed in equilibrium with βZr .

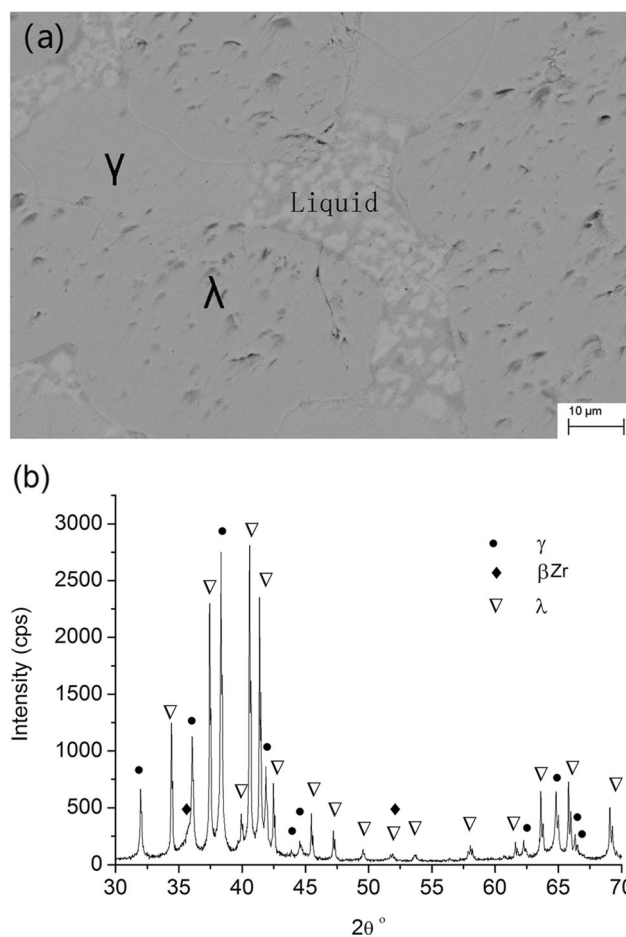


Fig. 4 (a) BSE image of microstructure, and (b) x-ray diffraction pattern of alloy 3 annealed at 1000 °C for 20 days

The compositions of the equilibrated phases are provided in Table 1.

Figure 4(a) shows a backscattered electron (BSE) image of alloy 3, where the co-existence of γ - $Zr_2(Mo,Fe)$, λ - $Zr(Mo,Fe)_2$, and solidified liquid can be observed. The domain where the white-gray phase mixes with the black-gray phase was the liquid phase. The white-gray phase has a βZr structure with a composition of $Zr_{92.1}Mo_{4.1}Fe_{3.8}$, while the black-gray phase has a Zr_2Fe structure with a composition of $Zr_{67.5}Mo_{0.3}Fe_{32.2}$. These phases are the solidification products of the liquid phase after quenching. Figure 4(b) shows the x-ray diffraction (XRD) pattern of this alloy, which is in agreement with the observations made using SEM/EDS. After being annealed at 1000 °C for 20 days, alloy 4 exhibited an equilibrium between γ - $Zr_2(Mo,Fe)$, β -Zr, and λ - $Zr(Mo,Fe)_2$, as can be seen in Fig. 5. The compositions of γ - $Zr_2(Mo,Fe)$, λ - $Zr(Mo,Fe)_2$ and βZr in this alloy are $Zr_{63.2}Mo_{12.0}Fe_{24.8}$, $Zr_{38.0}Mo_{39.0}Fe_{23.0}$ and $Zr_{89.5}Mo_{7.7}Fe_{2.8}$, respectively. Figure 5(b) shows the XRD pattern of this alloy, which is consistent with the observation made using SEM/EDS.

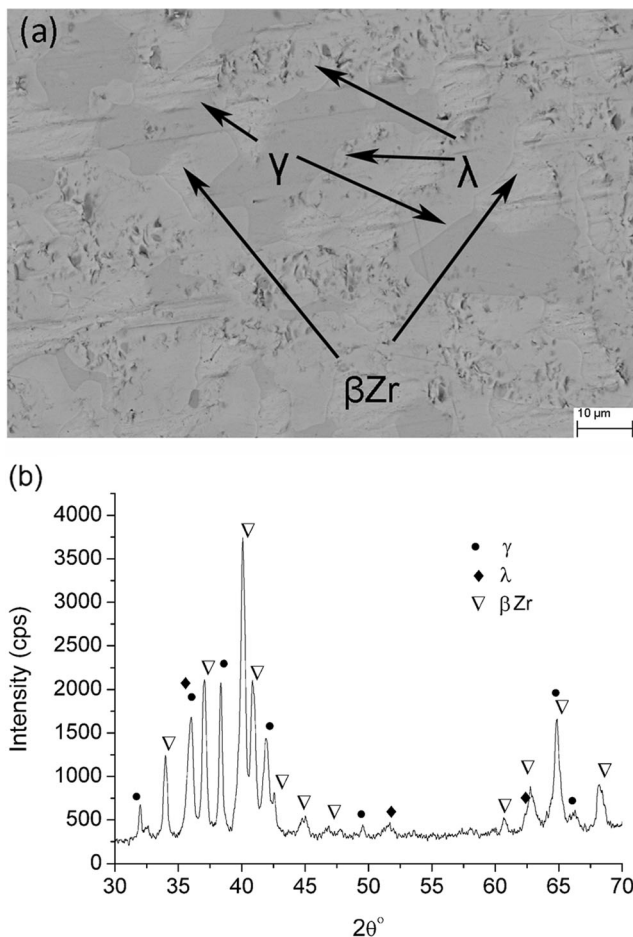


Fig. 5 (a) BSE image of microstructure, and (b) x-ray diffraction pattern, of alloy 4 annealed at 1000 °C for 20 days

Alloy 6 exhibits an equilibrium between $\gamma\text{-Zr}_2(\text{Mo,Fe})$, ZrMo_2 , and βZr , as shown in Fig. 6. The microstructures and x-ray diffraction patterns of this alloy confirm that $\gamma\text{-Zr}_2(\text{Mo,Fe})$ coexisted with ZrMo_2 and βZr . The XRD analysis verifies the existence of $\gamma\text{-Zr}_2(\text{Mo,Fe})$, ZrMo_2 , and βZr in this alloy. In alloy 9, an equilibrium among γ , λ , and ZrFe_2 phases was observed, as shown in Fig. 7. X-ray diffraction peaks of ZrFe_2 overlap with those of $\text{Zr}(\text{Mo,Fe})_2$. Identification of ZrFe_2 is mainly based on the composition analysis. It is worth noting that the presence of un-melted Mo was observed in alloy 5 due to the high melting point of molybdenum and the short melting time or insufficient melting current used. Along with Mo, $\gamma\text{-Zr}_2(\text{Mo,Fe})$, βZr , and ZrMo_2 phases were detected in this alloy, as shown in Fig. 8. With the exception of alloy 5, none of the fabricated alloys showed the presence of un-melted Mo.

Figure 9 displays the tie-triangles determined for alloys 4 and 6, where the tie-triangle of $[\gamma + \beta\text{Zr} + \lambda]$ partially overlaps with that of $[\gamma + \beta\text{Zr} + \text{ZrMo}_2]$. Likewise, the tie-triangles of $[\gamma + \lambda + \text{ZrFe}_2]$ and $[\gamma + \lambda + \text{liquid}]$ determined for alloys 3 and 9 are presented in Fig. 9 and

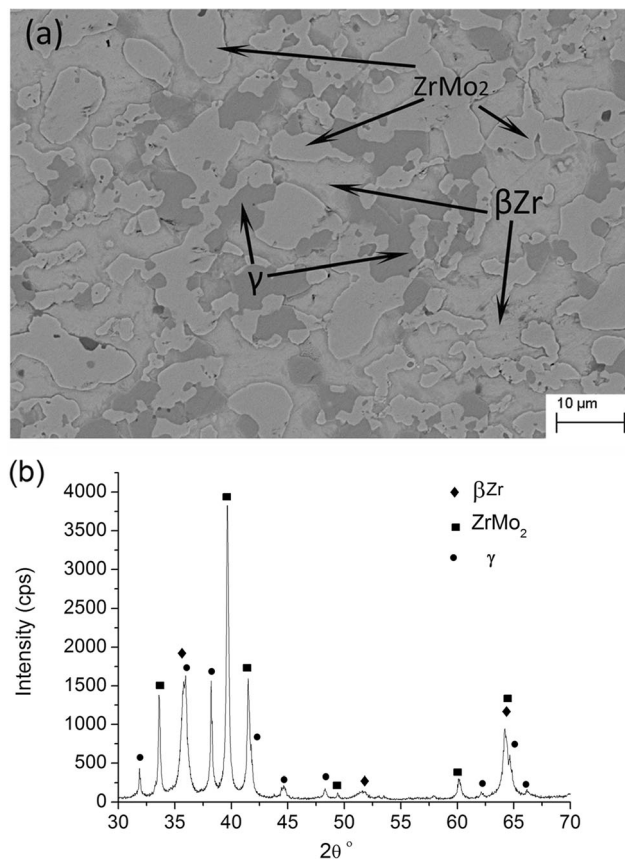


Fig. 6 (a) BSE image of microstructure, and (b) x-ray diffraction pattern, of alloy 6 annealed at 1000 °C for 20 days

overlap with each other as well. In the ternary Zr-Mo-Fe system, if equilibrium is attained after the heat treatment, a tie-triangle of either $[\gamma + \beta\text{Zr} + \lambda]$ or $[\gamma + \beta\text{Zr} + \text{ZrMo}_2]$ is anticipated for alloys 4 and 6. The same holds true for alloys 3 and 9. After being annealed for an additional 10 days, x-ray diffraction patterns of alloys 4 and 6 were found to remain unchanged. Well-defined phase boundaries in alloys 4 and 6 indicate that both alloys have attained equilibrium. The oxygen contents in alloys 2, 5 and 6 are 1200 ppm, 3400 ppm and 4800 ppm, respectively. Thus, oxygen is thought to be the reason of overlap of the tie-triangles.

Figure 10 shows the BSE image, x-ray diffraction, and element maps of alloy 15. This alloy ($\text{Zr}_{63}\text{Mo}_{13}\text{Fe}_{24}$) has a composition slightly different to that of alloy 1 ($\text{Zr}_{63}\text{Mo}_{12}\text{Fe}_{25}$) and was produced in a different melting batch. The aim was to investigate if it was possible to obtain βZr and $\lambda\text{-Zr}(\text{Mo,Fe})_2$ without the presence of $\gamma\text{-Zr}_2(\text{Mo,Fe})$ by carefully controlling the melting process to eliminate oxygen contamination. Unexpectedly, a four-phase equilibrium of liquid, βZr , $\gamma\text{-Zr}_2(\text{Mo,Fe})$, and $\lambda\text{-Zr}(\text{Mo,Fe})_2$ was observed in this alloy, as shown in Fig. 10(a). Upon quenching, the liquid solidified into a mixture of Zr_2Fe ,

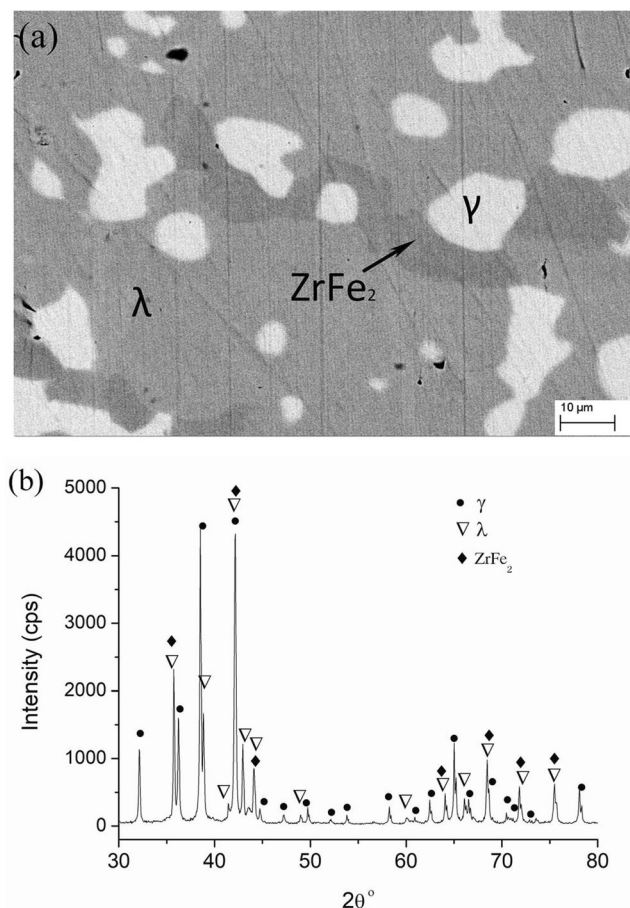


Fig. 7 (a) BSE image of microstructure, and (b) x-ray diffraction pattern, of alloy 9 annealed at 1000 °C for 5 days

βZr , and $\gamma\text{-Zr}_2(\text{Mo,Fe})$. The black area in the liquid domain represents Zr_2Fe . The compositions of the precipitates can be found in Table 1. Figure 10(c), (d), (e), (f) and (g) display the element maps of O, Zr, Fe, and Mo for this alloy. As shown in Fig. 10(c), oxygen preferred to segregate in βZr , regardless of whether it is an equilibrium phase or a solidification product. The equilibrium phases ranked by oxygen concentration from highest to lowest are βZr , liquid, $\gamma\text{-Zr}_2(\text{Mo,Fe})$, and λ . It is worth noting that a certain amount of oxygen dissolves in the γ phase, and oxygen in λ is negligible.

Figure 11 depicts the BSE image, x-ray diffraction, and element maps of alloy 16, in which equilibrium of $\gamma\text{-Zr}_2(\text{Mo, Fe})$, liquid, and $\lambda\text{-Zr}(\text{Mo,Fe})_2$ was observed. The element maps showed that oxygen preferred to segregate in liquid. Minor oxygen was detected in $\gamma\text{-Zr}_2(\text{Mo, Fe})$ and $\lambda\text{-Zr}(\text{Mo,Fe})_2$. The oxygen content in $\gamma\text{-Zr}_2(\text{Mo, Fe})$ is slightly higher than that in $\lambda\text{-Zr}(\text{Mo,Fe})_2$.

The oxygen content in alloy 2 was determined to be 1200 ppm. Area fractions of $\gamma\text{-Zr}_2(\text{Mo, Fe})$ and $\lambda\text{-Zr}(\text{Mo, Fe})_2$ in this alloy were measured to be 88 % and 12 %, respectively, and were directly treated as the volume

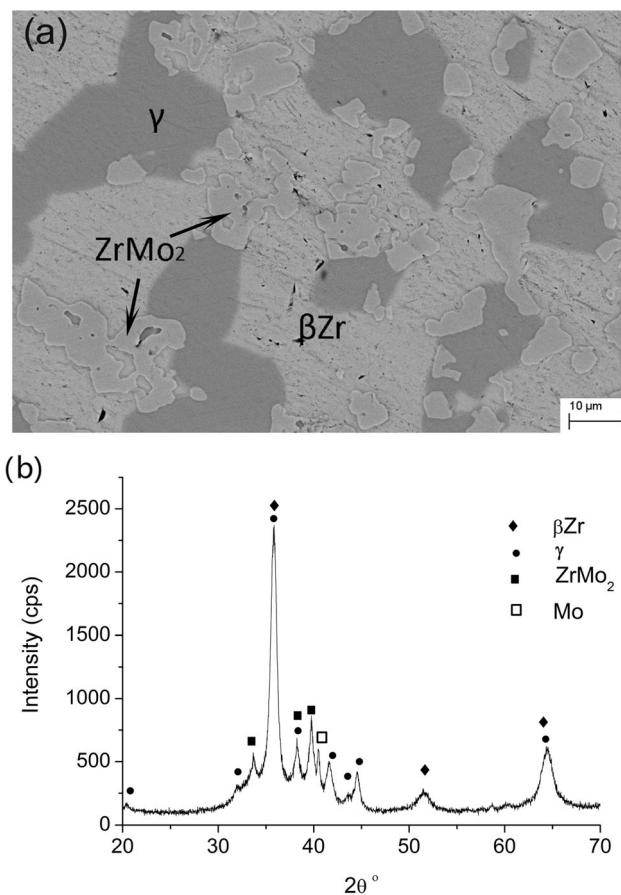


Fig. 8 (a) BSE image of microstructure, and (b) x-ray diffraction pattern, of alloy 5 annealed at 1000 °C for 20 days

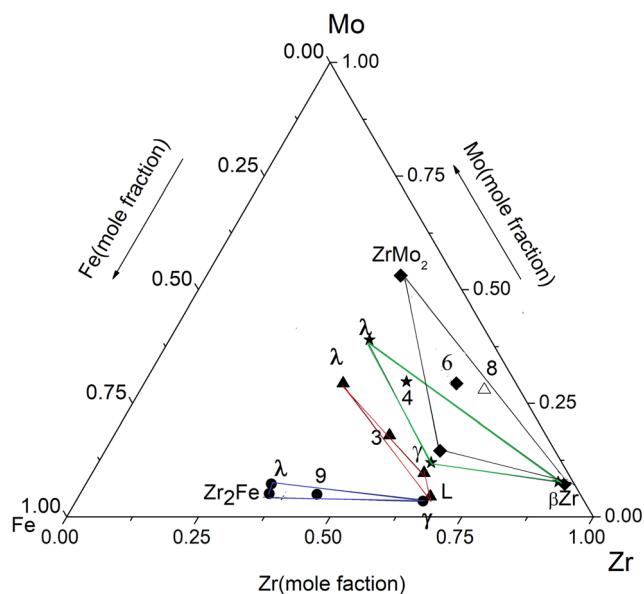


Fig. 9 Tie-triangle determined for alloys 4 and 6, alloys 3 and 9. Filled triangle: alloy 3, filled circle: alloy 9, filled star: alloy 4, filled rectangle: alloy 6. Empty triangle corresponds to alloy 8. Digits in the figure indicate the alloy composition

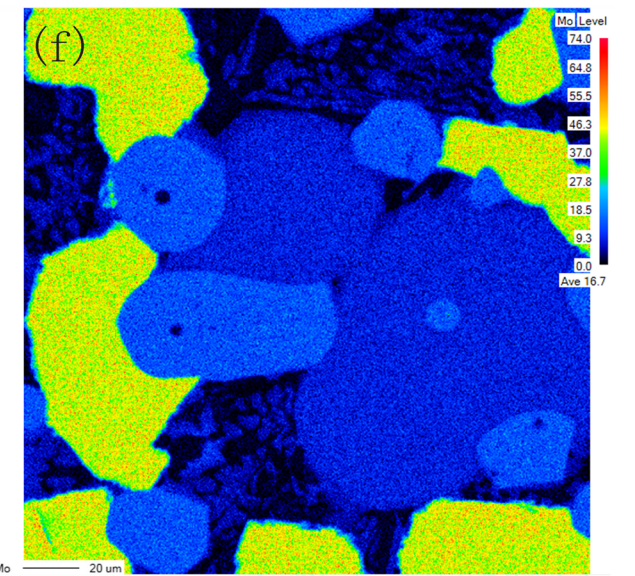
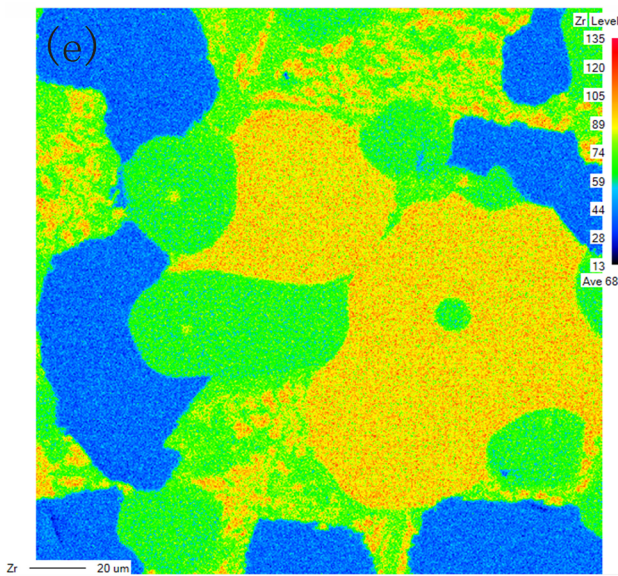
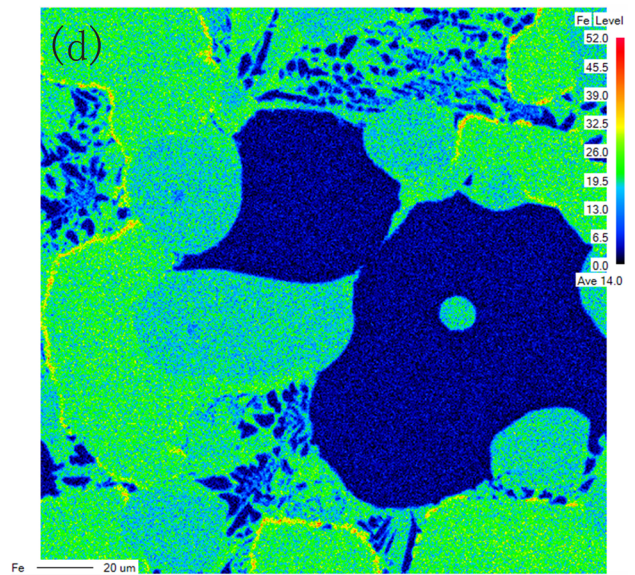
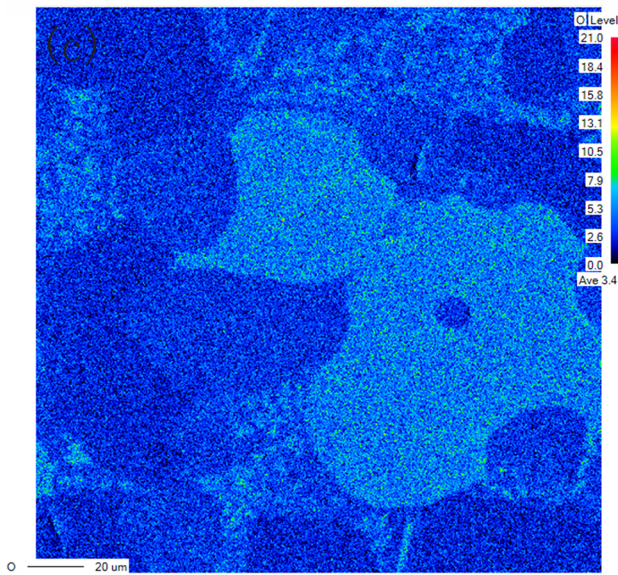
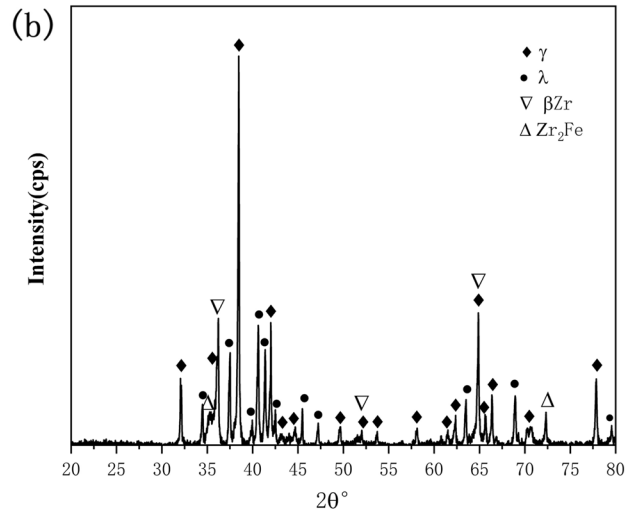
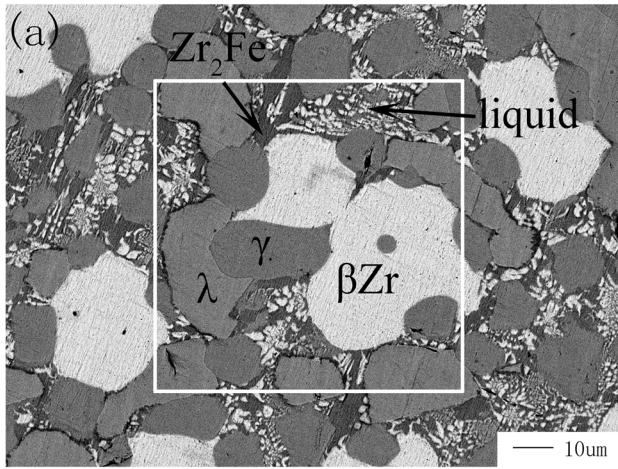


Fig. 10 The experimental results for alloy 15 annealed at 1000 °C for 7 days, (a) microstructure, (b) x-ray pattern, (c)–(f) Element maps of O, Fe, Zr, and Mo, respectively. The white square in Figure (a) defines the domain for element maps

fraction. The cell parameter of λ -Zr(Mo, Fe)₂ is $a = 0.507$ nm, $c = 0.833$ nm. The relative molecular weights and the densities of γ -Zr₂(Mo, Fe) and λ -Zr(Mo, Fe)₂ are 243 g/mol and 219 g/mol, and 7.12 g·cm⁻³ and 7.84 g·cm⁻³, respectively. The volume fractions for both phases were converted into mass fractions, which were 87% for γ -Zr₂(Mo, Fe), and 13% for λ -Zr(Mo, Fe)₂, respectively. The element maps of alloy 15 showed that oxygen in λ -Zr(Mo, Fe)₂ is nearly undetected, so it will not introduce significant error by assuming that all oxygen dissolves in γ -Zr₂(Mo, Fe) for alloy 2. Thus, the oxygen concentration in the γ -Zr₂(Mo, Fe) compound is calculated to be approximately 2.2 at. %.

Alloy 15 presents a microstructure of four-phase equilibrium of [β Zr, liquid, λ -Zr(Mo, Fe)₂, γ -Zr₂(Mo, Fe)]. β Zr, liquid, λ -Zr(Mo, Fe)₂ are stable equilibrium phases in the Zr-Mo-Fe alloy.^[18,19] Thus, it is reasonable to conclude that γ -Zr₂(Mo, Fe) is formed by the introduction of oxygen. This conclusion is also supported by the results of above element maps and the oxygen content calculation for γ -Zr₂(Mo, Fe). The designed composition of alloys 1 and 15 is nearly identical and very close to the measured composition of γ phase. Apart from phases γ , β Zr, and λ -Zr(Mo, Fe)₂, which were found in alloy 1, additional liquid appeared in alloy 15. This difference might be due to the varying oxygen content between alloys 1 and 15, as the oxygen uptake varied from alloy to alloy during the melting procedure.

The γ phase is an oxygen-stabilized compound in the Zr-Mo-Fe (O) system. Thus, results obtained from alloys 4 and 6 defined a four-phase equilibrium of [β Zr + λ -Zr(Mo, Fe)₂ + γ + ZrMo₂] in this quaternary system. The results obtained from alloys 3 and 9 specified another four-phase region [λ -Zr(Mo, Fe)₂ + γ + Liquid + ZrFe₂].

It is well known that impurities such as O and N can stabilize intermetallics Zr₂M (M = Fe, Co, Ni, etc.) and result in the formation of partially filled cubic Ti₂Ni structure-type ternary compounds, such as Zr₄Fe₂O,^[24] Zr₄Co₂O,^[25] Zr₄Ni₂O,^[26,27] and Zr₄Pt₂O.^[28] Two ternary compounds with similar composition and with identical Ti₂Ni structure, τ_1 (Zr₆₅Mo_{18-x}Ni_{16.5+x}) and ω (approximately Zr₆₆Mo₁₂Co₂₂), have been reported in the Zr-Mo-Ni and Zr-Mo-Co ternary systems, respectively.^[29,30] These compounds were treated as stable phase in these ternary systems. Given the similarity of the composition between γ -Zr₂(Mo, Fe), τ_1 (Zr₆₅Mo_{18-x}Ni_{16.5+x}) and ω (approximately Zr₆₆Mo₁₂Co₂₂),^[29,30] and the similarity of Fe, Co

and Ni, further work needs to be done to clarify whether τ_1 (Zr₆₅Mo_{18-x}Ni_{16.5+x}) and ω (approximately Zr₆₆Mo₁₂Co₂₂) are stabilized by oxygen.

To verify the existence of the ternary compound Zr₉Mo₄Fe, alloy 6 was designed to be located in the region where Zr₉Mo₄Fe equilibrates with λ -Zr(Mo, Fe)₂, based on the thermodynamical assessment of the Zr-Mo-Fe system.^[17] However, Zr₉Mo₄Fe was not observed in this alloy. To further verify the existence of Zr₉Mo₄Fe, additional alloy 8 with a nominal composition of Zr_{65.2}Mo_{28.0}Fe_{6.7}, nearly identical to the composition of Zr₉Mo₄Fe, was arc melted and subjected to heat treatment. The phase ZrMo₂ grains, the deep-gray phase γ -Zr₂(Mo, Fe), and the gray-matrix phase β Zr were observed in this alloy, as shown in Fig. 12. It is clear that Zr₉Mo₄Fe was not observed in this study. These results are consistent with recently reported isothermal section of the Zr-Mo-Fe ternary system at 1000 °C by Du et al.^[19] They also did not observe the Zr₉Mo₄Fe compound in their study.^[19]

The present results show that there are 3 four-phase regions in the Zr-Mo-Fe (O) system in Zr-rich portion at 1000 °C, which are [β Zr + λ -Zr(Mo, Fe)₂ + γ + ZrMo₂], [β Zr + λ -Zr(Mo, Fe)₂ + γ + Liquid], and [λ -Zr(Mo, Fe)₂ + γ + Liquid + ZrFe₂], respectively. Phase relationships in the Zr-Mo-Fe (O) system in the Zr-rich portion at 1000 °C were illustrated and projected along the oxygen composition direction, as presented in Fig. 13. The circles in Fig. 13 represent the compositions of identified phases in the investigated alloys. When referring to Fig. 13, it should be noted that the projected phase regions overlap each other. For instance, the four-phase region [β Zr + λ -Zr(Mo, Fe)₂ + γ + ZrMo₂], bounded by lines $ab \rightarrow bc \rightarrow cd \rightarrow da$, overlaps with the projection of the three-phase region [β Zr + λ -Zr(Mo, Fe)₂ + γ], which is bounded by lines $be \rightarrow ef \rightarrow fh \rightarrow hd \rightarrow db$. Similarly, the projections of the three-phase region [β Zr + λ -Zr(Mo, Fe)₂ + γ] and four-phase region [β Zr + λ -Zr(Mo, Fe)₂ + γ + Liquid] overlap each other, too. It is important to note that the end-points of the tie-tetrahedron in Fig. 13 were arbitrarily determined. Excluding the oxygen-stabilized γ phase, tie-triangles in the oxygen-free Zr-Mo-Fe system in Zr-rich portion at 1000 °C are [β Zr + λ -Zr(Mo, Fe)₂ + ZrMo₂], [β Zr + λ -Zr(Mo, Fe)₂ + Liquid], and [λ -Zr(Mo, Fe)₂ + Liquid + ZrFe₂].

One of the interesting findings of this study is the presence of the oxygen-stabilized compound γ -Zr₂(Mo, Fe) in all investigated alloys, regardless of the phase region they are located in. Research on the oxidation of the Zr-base alloys mainly focused on the oxidation of Zr-matrix and its precipitates.^[31] However, there has been limited research on how the nature of the precipitates changes during the oxidation process. This discovery serves as a reminder that γ -Zr₂(Mo, Fe) may form in Zr-Mo-Fe based

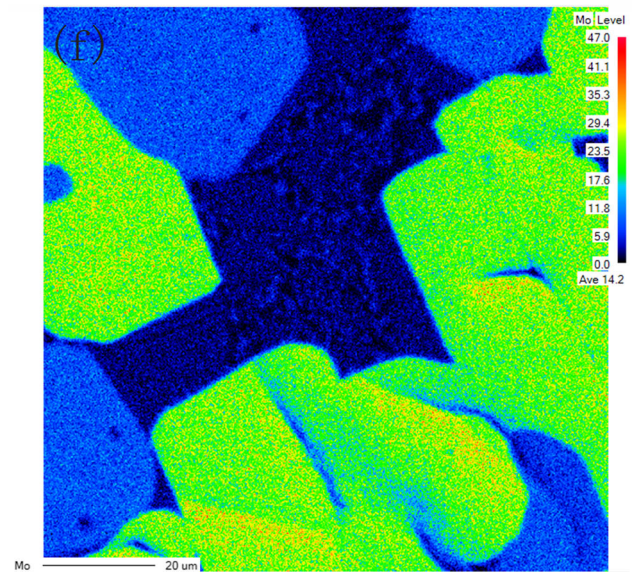
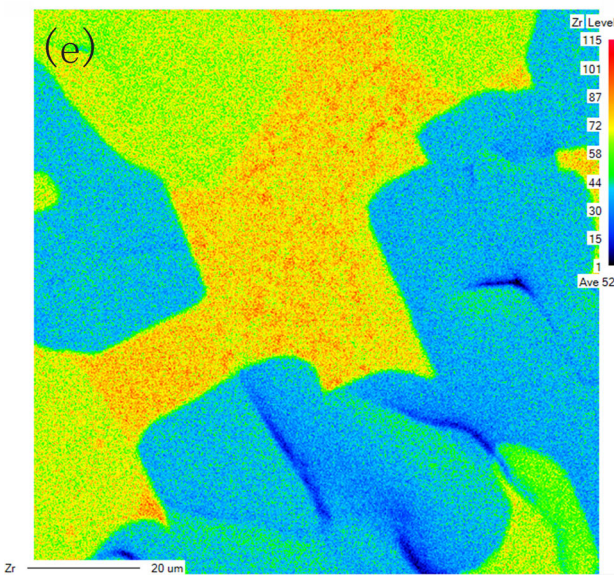
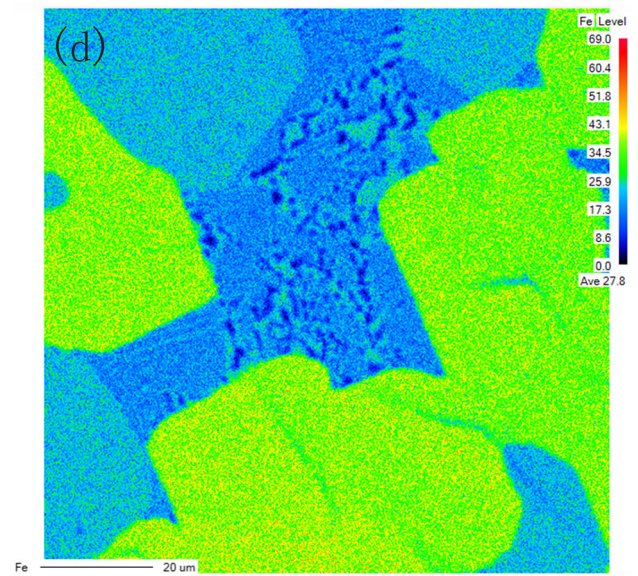
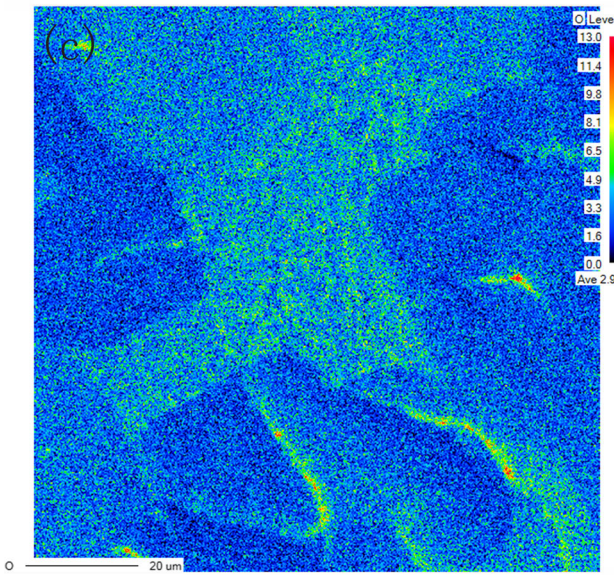
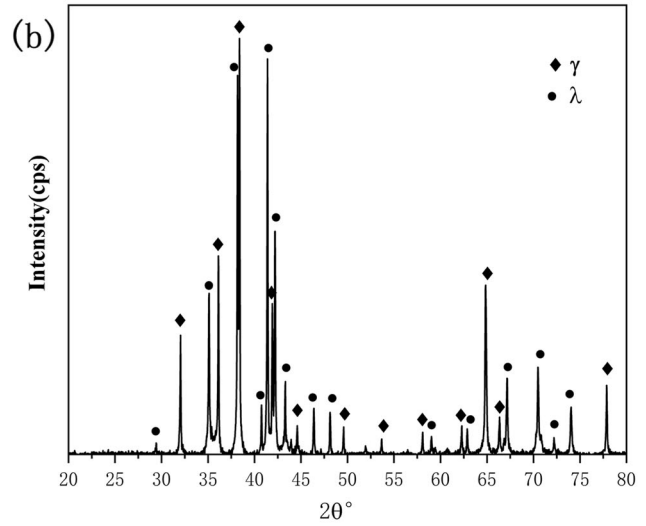
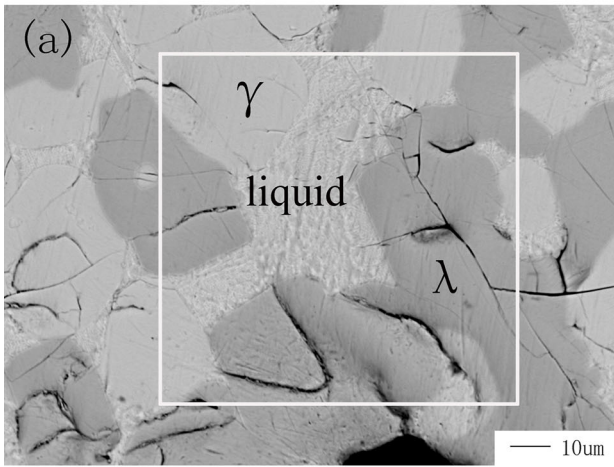


Fig. 11 The experimental results for alloy 16 heated at 1000 °C for 7 days, (a) microstructure, (b) x-ray pattern, (c)–(f) Element maps of O, Fe, Zr, and Mo, respectively. The white square in Figure (a) defines the domain for element maps

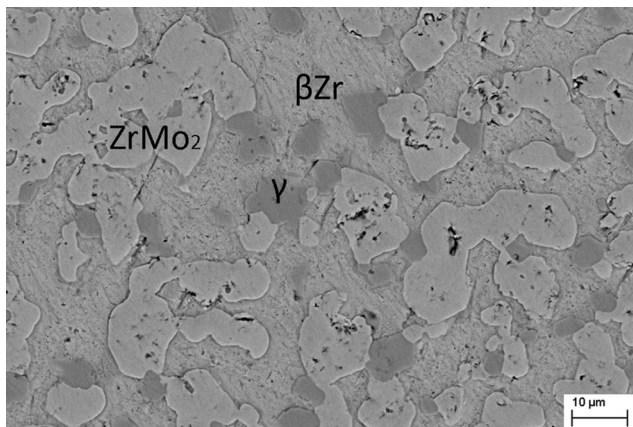


Fig. 12 Microstructure of alloy 8 annealed at 1000 °C for 20 days

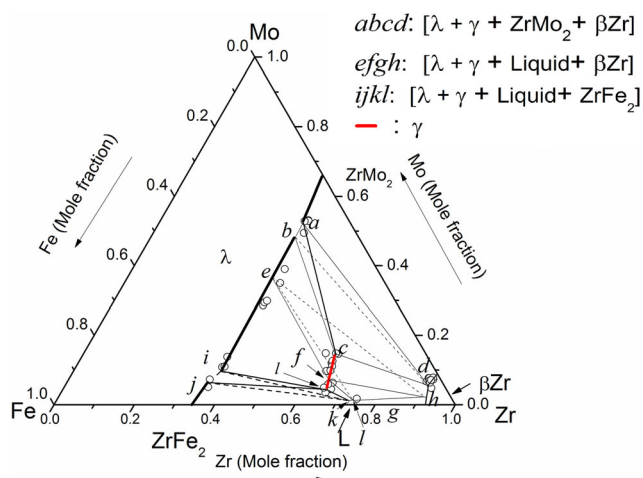


Fig. 13 Phase relationships of the Zr-Mo-Fe (O) system in the Zr-rich corner at 1000 °C—Projection along the oxygen composition direction. Along the projection direction, the solid lines represent the visible edges of equilibrium tetrahedron, and the dashed lines represent the hidden edges of equilibrium tetrahedron

alloys as the ingress of oxygen increases during service. The current element mapping has shown that oxygen tends to segregate in the β Zr phase, while minor or very limited oxygen was observed in the intermetallics. This result is consistent with the oxidation process of zirconium-based alloys, in which zirconium prefers to oxidize and the intermetallics exhibit delayed oxidation.^[32]

Based on the compositions listed in Table 1, the maximum solubilities of Mo in the $ZrFe_2$ and Fe in $ZrMo_2$, are 5 at.% and 12 at.%, respectively. The solubility of Mo in

$ZrFe_2$ in this study is quite consistent with that (4.9 at.%) reported in Ref 19. The composition range of λ -Zr(Mo,Fe)₂ varies from 7 to 39 at.% Mo with Zr at approximately constant 36 at.%. Current composition range of λ -Zr(Mo,Fe)₂ is consistent with that reported by Du et al., which is 8–40.7 at.% Mo.^[19]

4 Conclusions

- (1) When the amount of oxygen increases in the Zr-Mo-Fe alloys, a oxygen-stabilized compound was observed to be present in this system. This compound was identified as γ -Zr₂(Mo,Fe) with cell parameter of $a = 1.2213$ nm, with an approximate composition of $Zr_{63}Mo_{12}Fe_{25}$.
- (2) The previously reported ternary compound Zr_9Mo_4Fe was not observed in the current work.
- (3) For the Zr-Mo-Fe (O) system at 1000 °C, three four-phase regions, which are $[\beta Zr + \lambda\text{-Zr}(\text{Mo,Fe})_2 + \gamma + ZrMo_2]$, $[\beta Zr + \lambda\text{-Zr}(\text{Mo,Fe})_2 + \gamma + \text{Liquid}]$, and $[\lambda\text{-Zr}(\text{Mo,Fe})_2 + \gamma + \text{Liquid} + ZrFe_2]$, are identified in the Zr-rich corner.

Acknowledgment This project is supported by Guangxi Natural Science Foundation (Grant No. 2018GXNSFAA138043), Open Foundation of Guangxi Key Laboratory of Processing for Non-ferrous Metals and Featured Materials, Guangxi University (Grant No. GXYSF01803), Guangxi Provincial Science and Technology (Grant No. 2020KY04026, 2022KY0150), Natural Science Foundation of Guangdong Province (2022A1515010919, 2023A1515012089), and the Special Projects of Universities in Guangdong Province in Key Areas (2022ZDZX3014).

References

1. A.T. Motta, Waterside Corrosion in Zirconium Alloys, *JOM*, 2011, **63**(8), p 63–67.
2. J.P. Abriata, J. Garcés, and R. Versaci, The O-Zr (Oxygen-Zirconium) system, *Bull. Alloy Phase Diagr.*, 1986, **1986**(7), p 116–124.
3. M. Billone, Y. Yan, T. Burtseva, R. Daum, Cladding Embrittlement during Postulated Loss-of-Coolant Accidents, NUREG/CR-6967, July 31, 2008; United States. (<https://digital.library.unt.edu/ark:/67531/metadc901576/>)
4. G. Hache and H.M. Chung, The History of LOCA Embrittlement Criteria, NUREG/CP-0172, pp. 205–237 (2001)
5. M. Slobodyan, Arc Welding of Zirconium and Its Alloys: A Review, *Prog. Nucl. Energy*, 2021, **133**, p 103630.
6. M. Pahutova, K. Kucharova, and J. Cadek, Creep and Creep Fracture in Zr-Sn-Mo and Zr-Sn-Mo-Nb Alloys at Temperatures of 623–823 K—II, *Creep Fract. Kovove Mater.*, 1976, **14**(6), p 702–716.
7. M. Pahutová, J. Čadek, and V. Černý, Creep and Creep Rupture of a Zr-6%Sn-1%Mo Alloy, *J. Nucl. Mater.*, 1977, **68**(1), p 111–121.

8. M. Pahutová, and J. Čadek, Effect of Molybdenum on Some Basic Creep Characteristics of Alpha Zirconium in a Temperature Interval of 350 to 600 °C, *Mater. Sci. Eng. C*, 1975, **20**, p 277–285.
9. B. Cheadle, R. Holt, V. Fidleris, A. Causey, V. Urbanic, High-strength, creep-resistant excel pressure tubes, zirconium in the nuclear industry. in 4–7 Aug. 1980 (Boston), ASTM Committee B-10 on Reactive and Refractory Metals and Alloys (Sponsor), ed. by D. Franklin, West Conshohocken, PA, ASTM International, pp. 193–207 (1982).
10. J.H. Lee, and S.K. Hwang, Effect of Mo Addition on the Corrosion Resistance of Zr-Based Alloy in Water Containing LiOH, *J. Nucl. Mater.*, 2003, **321**(2), p 238–248.
11. A.V. Nikulina, V.F. Konkov, M.M. Peregud, and E.E. Vorobev, Effect of Molybdenum on Properties of Zirconium Components of Nuclear Reactor Core, *Nucl. Mater. Energy*, 2018, **14**, p 8–13.
12. J. Liang, H. Yu, A. Barry, E.C. Corcoran, L. Balogh, and M.R. Daymond, Re-investigation of Phase Transformations in the Zr-Excel Alloy, *J. Alloys Compd.*, 2017, **716**, p 7–12.
13. F. Stein, G. Sauthoff, and M. Palm, Experimental Determination of Intermetallic Phases, Phase Equilibria, and Invariant Reaction Temperatures in the Fe-Zr System, *J. Phase Equilib.*, 2002, **23**(6), p 480–494.
14. R.J. Perez, and B. Sundman, Thermodynamic Assessment of the Mo-Zr Binary Phase Diagram, *Calphad*, 2003, **27**(3), p 253–262.
15. A.F.A. Guilletmet, The Fe-Mo (Iron-Molybdenum) System, *Bull. Alloy Phase Diagr.*, 1982, **3**(3), p 359–367.
16. N.M. Gruzdeva, T.A. Tregubov, ЖЕЛЕЗО–МОЛИБДЕН–ЦИРКОНИЙ (Iron-Molybdenum-Zirconium), Диаграммы состояния металлических систем (State Diagrams of Metal Systems), Алисова С.П., Будберг П.Б., Агеев Н.В. (ред) опубликованные в 1968 году, Выпуск 14, p 188. (In Russia) Alisova S.P., Budberg P.B., Ageev N.V. (ed), published in 1968, Issue 14, p. 188.
17. P. Rogl, H. Nowotny, and F. Benesovsky, New K-Borides and Related Phases (Filled up Re₃B-Phases), *Mon. Chem.*, 1973, **104**(1), p 182–193.
18. M. Zinkevich, and N. Mattern, Thermodynamic Modeling of the Fe-Mo-Zr System, *Acta Mater.*, 2002, **50**(13), p 3373–3383.
19. Z. Du, L. Zou, C. Guo, X. Ren, and C. Li, Experimental Investigation and Thermodynamic Description of the Fe-Mo-Zr System, *Calphad*, 2021, **74**, p 102314.
20. A. Boultif, and D.J. Louër, Indexing of Powder Diffraction Patterns for Low-Symmetry Lattices by the Successive Dichotomy Method, *J. Appl. Crystallogr.*, 1991, **24**, p 987–993.
21. A. Boultif, and D. Louër, Powder Pattern Indexing with the Dichotomy Method, *J. Appl. Crystallogr.*, 2004, **37**, p 724–731.
22. D. Louër, and A. Boultif, Indexing with the Successive Dichotomy Method, DICVOL04, *Z. Kristallogr. Suppl.*, 2006, **23**, p 225–230.
23. J. Schindelin, I. Arganda-Carreras, E. Frise, V. Kaynig, M. Longair, T. Pietzsch, and A. Cardona, Fiji: An Open-Source Platform for Biological-Image Analysis, *Nat. Methods*, 2012, **9**(7), p 676–682.
24. International Centre for Diffraction Data, 12 Campus Boulevard, Newtown Square, PA 19073–3273, USA.
25. A.A. Lavrentyeva, B.V. Gabrelian, P.N. Shkumat, I.Y. Nikiforov, I.Yu. Zavaliy, and O.Yu. Khyzhun, Electronic Structure of Zr₄Fe₂O: Ab Initio APW+LO Calculations and x-ray Spectroscopy Studies, *J. Phys. Chem. Solid.*, 2013, **74**, p 590–594.
26. H. Holleck, and F. Thummler, Ternäre Komplex-Carbide, -Nitride und -Oxide Mit Teilweise Aufgefüllter Ti₂Ni-Struktur, *Monatsch. Chem.*, 1967, **98**, p 133–134.
27. R. Mackay, G.J. Miller, and H.F. Franzen, New Oxides of the Filled-Ti₂Ni Type Structure, *J. Alloys Compd.*, 1994, **204**(1–2), p 109–118.
28. S. Gupta, D.J. Sordet, and J.D. Corbett, Structural and Compositional Investigations of Zr₄Pt₂O: A Filled-Cubic Ti₂Ni-Type Phase, *J. Solid State Chem.*, 2009, **182**, p 1708–1712.
29. S. Wang, C. Zhang, C. Lin, Y. Peng, and Y. Du, Measurement of 900 °C Isothermal Section in the Mo-Ni-Zr System, *J. Phase Equilib. Diffus.*, 2016, **37**(5), p 672–679.
30. C. Lin, C. Zhang, S. Wang, P. Zhou, and Y. Du, Phase Equilibria of the Co-Mo-Zr Ternary System at 1000 °C, *J. Phase Equilib. Diffus.*, 2018, **39**(5), p 510–518.
31. J. Sayers, S. Lozano-Perez, and S.R. Ortner, The Progress of SPP Oxidation in Zircaloy-4 and Its Relation to Corrosion and Hydrogen Pickup, *Corros. Sci.*, 2019, **158**, p 108972.
32. C. Proff, S. Abolhassani, and C. Lemaignan, Oxidation Behaviour of Zirconium Alloys and Their Precipitates—A Mechanistic Study, *J. Nucl. Mater.*, 2013, **432**(1–3), p 222–238.

Publisher's Note Springer Nature remains neutral with regard to jurisdictional claims in published maps and institutional affiliations.

Springer Nature or its licensor (e.g. a society or other partner) holds exclusive rights to this article under a publishing agreement with the author(s) or other rightsholder(s); author self-archiving of the accepted manuscript version of this article is solely governed by the terms of such publishing agreement and applicable law.